Materials Advances

ROYAL SOCIETY OF CHEMISTRY

PAPER

View Article Online
View Journal

Cite this: DOI: 10.1039/d6ma00364h

Composition-dependent plasmon-enhanced emission in lead-free $Cs_3Cu_2X_5$ halide LEDs: a DFT-FDTD study

Shoumik Debnath,[a] Sudipta Saha,[a] Khondokar Zahin,[a] Ying Yin Tsui[b] and Md Zahurul Islam *[a]

Lead-free $Cs_3Cu_2X_5$ (X = Cl, Br, I) halides show high photoluminescence quantum yields (PLQYs) and good ambient stability, yet LEDs based on these materials still suffer from poor optical outcoupling. In this work, we combine density functional theory (DFT) and finite-difference time-domain (FDTD) simulations to optimize plasmonic enhancement in $Cs_3Cu_2X_5$ LEDs using composition-specific optical constants. First-principles calculations provide a wavelength-dependent refractive index and extinction coefficient data for each halide. These values are then used in FDTD to model a complete device stack with Ag/SiO_2 core–shell nanostructures. Out of the three halides, $Cs_3Cu_2Cl_5$ performs best with 4.4× Purcell enhancement and 30% light extraction using optimized nanorods. The chloride outperforms the others due to its lower refractive index ($n \approx 1.9$). $Cs_3Cu_2Br_5$ has the highest spectral overlap (95.5%) but only moderate extraction efficiency (26%) because of increased optical confinement. For $Cs_3Cu_2I_5$, a nanosphere geometry is required due to its emission wavelength. But, the extraction efficiency remains limited to approximately 10% even with moderate Purcell enhancement. The optimal separation between the emitter and plasmon depends on the material composition. For $Cs_3Cu_2Br_5$, this distance is 8–12 nm, while $Cs_3Cu_2Cl_5$ requires approximately 15 nm. These results provide composition-specific design guidelines for plasmon-enhanced lead-free LEDs.

Received 15th March 2026,
Accepted 9th May 2026

DOI: 10.1039/d6ma00364h

rsc.li/materials-advances

1 Introduction

Metal halide perovskite LEDs have advanced rapidly over the past decade. Red emitters now hit 28% external quantum efficiency (EQE),[1] green devices reach 30%,[2] and blue recently crossed 23%.[3] These numbers rival state-of-the-art OLEDs.[4,5] The performances are achieved due to high absorption coefficients, tunable emission across visible to near-infrared wavelengths, narrow linewidths below 20 nm, and high photoluminescence quantum yields.[6–8] However, two fundamental problems remain. First, lead toxicity blocks commercialization.[9–11] Second, even high-yield emitters lose roughly 80% of the generated photons to waveguide and substrate modes.[12–14] Simply replacing lead will not solve the photon extraction bottleneck. Despite rapid progress in device efficiency, existing approaches largely treat material development and optical design as separate problems, which limits the ability to achieve simultaneous improvements in stability and light extraction.

Early lead-free efforts targeted tin and germanium perovskites because Sn^{2+} and Ge^{2+} mimic the Pb^{2+} valence configuration.[9,15] Tin-based PeLEDs have reached EQEs near 20%.[7] But both cations oxidize rapidly to tetravalent states under ambient conditions, creating deep-level defects that kill emission within hours.[7,9,16] Tin is especially unstable due to its low Sn^{2+}/Sn^{4+} redox potential of +0.15 V.[16] For commercial viability, devices need to operate beyond 10 000 hours.[17] Neither lead-based nor current lead-free systems meet this requirement alongside cost and safety constraints.

The optical extraction problem persists regardless of the emitter material. Halide perovskites have refractive indices around 2.5,[4,14,18] which limits outcoupling efficiency to roughly 8%.[4] Total internal reflection alone accounts for about 56% of radiative power loss.[13,14] Fixing these losses requires accurate wavelength-dependent optical constants, specifically the refractive index (n) and extinction coefficient (k), which vary with composition and emission energy.[19,20] Most optical models use generic n and k datasets that cause spectral mismatch between photoluminescence and cavity resonances.[19,21] Without composition-specific dispersion data, device optimization remains empirical rather than predictive.

These challenges share a common root. Material development and photonic engineering have been treated as separate

[a] Department of Electrical and Electronic Engineering, Bangladesh University of Engineering and Technology, Dhaka 1000, Bangladesh. E-mail: mdzahurulislam@eee.buet.ac.bd
[b] Department of Electrical and Computer Engineering, University of Alberta, Edmonton, AB T6G 2H5, Canada

problems.[22] Synthetic chemists optimize composition for stability without comprehensive optical characterization.[23] Device engineers use placeholder optical constants that may not match the actual material.[24] The result is incomplete solutions. Materials that resist degradation can still suffer from poor photon extraction. High-PLQY emitters placed in optically mismatched environments underperform. Real progress requires tackling both issues together. As a result, there is a lack of predictive frameworks that directly connect composition-dependent material properties with device-level optical performance, particularly for emerging lead-free systems.

Copper-based halides with the $Cs_3Cu_2X_5$ stoichiometry (X = Cl, Br, I) offer a promising path forward. Unlike conventional three-dimensional ABX_3 perovskites, $Cs_3Cu_2X_5$ has a zero-dimensional crystal structure consisting of isolated $[Cu_2X_5]^{3-}$ bi-octahedral dimers separated by cesium cations.[25,26] This arrangement confines excitons to individual molecular units. The monovalent Cu^+ ($3d^{10}$) configuration provides a closed-shell electronic structure that resists oxidation, eliminating the instability pathways that plague Sn^{2+} and Ge^{2+} systems.[27–29] As a result, $Cs_3Cu_2X_5$ films maintain structural and optical integrity for weeks under ambient conditions without encapsulation.[26,30] Recent work has reported PLQYs approaching 95%,[27,31] with emission tunable from blue to near-infrared through halide substitution.[28,32] $Cs_3Cu_2Cl_5$ emits blue-green around 440 to 520 nm,[31,33] $Cs_3Cu_2Br_5$ emits green-yellow around 540 to 580 nm,[32] and $Cs_3Cu_2I_5$ emits in the green region around 530 to 550 nm.[28,34] Strong electron–phonon coupling within the isolated dimers produces self-trapped excitons with broadband emission and large Stokes shifts around 200 to 600 meV.[27,35] Still, PeLEDs using these materials show modest EQEs around 1 to 5%.[36] Chemical stability alone does not guarantee good device performance. Despite their high intrinsic photoluminescence efficiency and excellent stability, devices based on $Cs_3Cu_2X_5$ still suffer from poor light extraction, which limits their practical performance. This reveals a critical gap between material-level advantages and device-level efficiency that has not yet been systematically addressed.

Addressing the optical extraction challenge requires computational methods that bridge material-scale dispersion and device-scale electromagnetics.[24] First-principles DFT calculations using hybrid functionals like HSE06 with spin–orbit coupling provide accurate band structures and dielectric functions.[37,38] The resulting wavelength-dependent n and k spectra capture intrinsic material dispersion without relying on extrapolated values.[39] However, DFT describes bulk properties and cannot model electromagnetic field dynamics within multilayer device architectures.[22,25] The FDTD method fills this gap by solving Maxwell's equations numerically in space and time.[14,40] Importing DFT-derived optical constants into FDTD device models allows physically consistent evaluation of the Purcell factor, light extraction efficiency, spectral overlap, and far-field profiles.[41]

Recent first-principles studies on related lead-free halide systems have investigated the electronic structure and optical constants using similar DFT-based approaches.[42–44] These works confirm that GGA-PBE frameworks can reliably capture qualitative optical trends across halide compositions. However, they largely focus on material-level property characterization and do not link composition-dependent optical constants to device-level plasmonic performance.

Beyond passive optical engineering, plasmonic coupling through embedded metallic nanostructures offers active enhancement of light extraction.[12] Noble-metal nanoparticles support localized surface plasmon resonances that concentrate electromagnetic fields at the nanoscale and accelerate radiative recombination.[45] Gold nanorods combine excellent chemical stability with tunable plasmon resonances. Their longitudinal mode can be engineered through aspect-ratio control to align with $Cs_3Cu_2X_5$ emission, achieving strong spectral overlap and Purcell enhancement.[46,47] But accurate design of plasmon-emitter coupling requires composition-specific optical constants to predict resonance alignment at the nanoscale. However, most existing studies rely on simplified or literature-based optical parameters, which limits the reliability of plasmonic optimization and prevents systematic comparison across different material compositions.

Despite growing interest in lead-free perovskites, systematic studies linking halide composition, optical constants, and plasmonic performance remain scarce.[48] Prior research has largely focused on structural stability or bandgap tuning for photovoltaic applications.[25] In addition, most plasmonic simulations rely on generalized n and k datasets, which can lead to inaccurate predictions due to spectral mismatch.[49] As a result, a quantitative and composition-dependent understanding of the relationship between halide chemistry, optical dispersion, plasmon resonance alignment, and device-level performance is still lacking for $Cs_3Cu_2X_5$ systems.[48] To the best of our knowledge, a unified and composition-specific framework that integrates first-principles-derived optical constants with device-scale plasmonic simulations for $Cs_3Cu_2X_5$ systems has not yet been reported, limiting predictive optimization of these materials for light-emitting applications.

Here, we develop a fully integrated DFT-FDTD framework that establishes quantitative links between halide composition, wavelength-dependent optical properties, and plasmonic enhancement in $Cs_3Cu_2X_5$-based PeLEDs. Composition-specific n and k spectra derived from DFT are directly implemented in FDTD simulations that model emission enhancement, nanorod-emitter coupling, and far-field radiation. We further optimize Ag-nanorod geometries to maximize light extraction efficiency (LEE), Purcell factor, and spectral overlap. This integrated approach combines the chemical stability of copper-based halides with engineered photonic control, providing a predictive design pathway from atomic composition to device-level light extraction.

2 Methodology and theoretical background

2.1 DFT methodology

We carried out all density functional theory calculations using the CASTEP code. We treated exchange–correlation effects with the PBE functional within the generalized gradient approximation

framework. Ultrasoft pseudopotentials described the interactions between ions and electrons. We treated the following valence electron configurations explicitly: cesium $6s^1$, copper $3d^9 4s^2$, chlorine $3s^2 3p^5$, bromine $4s^2 4p^5$, and iodine $5s^2 5p^5$. We expanded the electronic wavefunctions using a plane-wave basis set with a kinetic energy cutoff of 450 eV. For Brillouin zone integration, we used a $6 \times 6 \times 6$ Monkhorst–Pack *k*-point grid.

We obtained starting structures from experimentally determined orthorhombic unit cells in the *Pnma* space group. Each unit cell contained 40 atoms. We relaxed both lattice vectors and atomic positions for all three halide compositions using the BFGS optimization algorithm. We continued the relaxation until the total energy changes dropped below 1×10^{-5} eV per atom, residual forces fell under 0.03 eV $Å^{-1}$, and atomic displacements stayed within 0.001 Å. These tight thresholds ensured well-converged ground state geometries.

After obtaining relaxed structures, we computed electronic band structures and density of states. We kept the same *k*-point mesh and smearing parameters from the ground state runs for consistency. We plotted band dispersions along the standard high-symmetry path for orthorhombic crystals, going through Γ, Z, Y, T, S, X, U, and R points in sequence. We set the Fermi level to zero energy in all plots. We then calculated the optical properties from the frequency-dependent dielectric function. We evaluated the dielectric response for photon energies spanning 0 to 20 eV using the independent particle approximation. This approach captures interband transitions that govern absorption and refractive index behavior in the visible and ultraviolet ranges. The optical properties were calculated using the GGA-PBE functional. The excitonic effects were not included, as they are expected to be relatively weak in bulk systems and do not significantly influence the overall optical trends (Fig. 1).

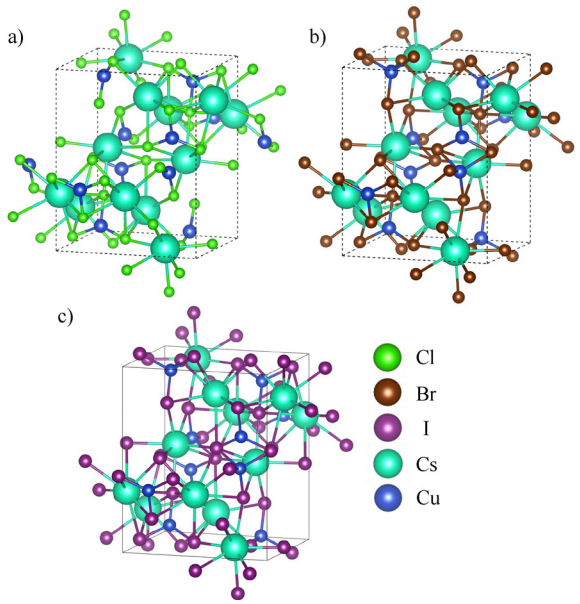

Fig. 1 Crystal structure of $Cs_3Cu_2X_5$ (a) X = Cl, (b) X = Br, and (c) X = I. The green, brown, violet, sky blue, and blue atom colors correspond to Cl, Br, I, Cs, and Cu atoms, respectively.

2.2 FDTD simulation setup

We modeled the optical behavior of plasmonic $Cs_3Cu_2X_5$ LEDs using three-dimensional FDTD simulations in Lumerical (Ansys Inc.).[50] Fig. 2 shows the computational workflow.

We designed the device stack to match experimentally reported LED architectures.[51] Starting from the bottom, we used 100 nm of ITO as the anode. On top of that we placed a 35 nm Spiro-OMeTAD hole transport layer. The 50 nm $Cs_3Cu_2X_5$ active layer came next, followed by 40 nm of ZnO as the electron transport layer. A 100 nm Ag film served as the top cathode. We imported the refractive index and extinction coefficient spectra for each $Cs_3Cu_2X_5$ composition directly from our DFT results. These wavelength-dependent optical constants ensure physically consistent coupling between the material-level electronic structure and device-level electromagnetic response. For the other device layers, we used optical constants from published literature.[52–54]

We placed an electric dipole source inside the perovskite layer to represent spontaneous emission. The dipole radiated across visible wavelengths matching the photoluminescence range of $Cs_3Cu_2X_5$. We positioned this source a few nanometers away from the plasmonic nanostructure surface to capture near-field coupling effects.[55] This placement allows accurate evaluation of emitter–plasmon coupling through modification of the local density of optical states (LDOS), which governs the Purcell enhancement.

We chose boundary conditions to balance physical accuracy with computational efficiency. Along the lateral *x* and *y* directions, we applied periodic boundaries to simulate an extended array of emitters. In the vertical *z* direction, we used perfectly matched layers to absorb outgoing waves and prevent artificial reflections from the simulation edges.[56] This combination ensures realistic modeling of an optically infinite device in-plane while eliminating non-physical reflections along the propagation direction.

We used a non-uniform spatial mesh throughout the simulation domain. We refined the grid spacing to 0.5–1 nm near the metal nanostructure and dipole region where field gradients are steepest. This fine mesh resolution is critical for accurately resolving localized surface plasmon resonances and strong near-field enhancements. We increased the mesh spacing away from these areas to reduce memory consumption.

We ran each simulation for 1500 fs, which gave the electromagnetic fields enough time to decay fully before we performed Fourier transforms to extract spectral data. Convergence of the results was verified with respect to both mesh size and simulation time, ensuring numerical stability and accuracy of the extracted optical quantities. Furthermore, the obtained Purcell factors and light extraction efficiencies are consistent with previously reported plasmon-enhanced perovskite systems, providing additional validation of the simulation framework.

2.3 Plasmonic nanostructure design

We selected the nanoparticle geometry based on spectral overlap optimization between the localized surface plasmon resonance (LSPR) and the emission wavelength of each perovskite composition. Nanorods offer a tunable longitudinal plasmon

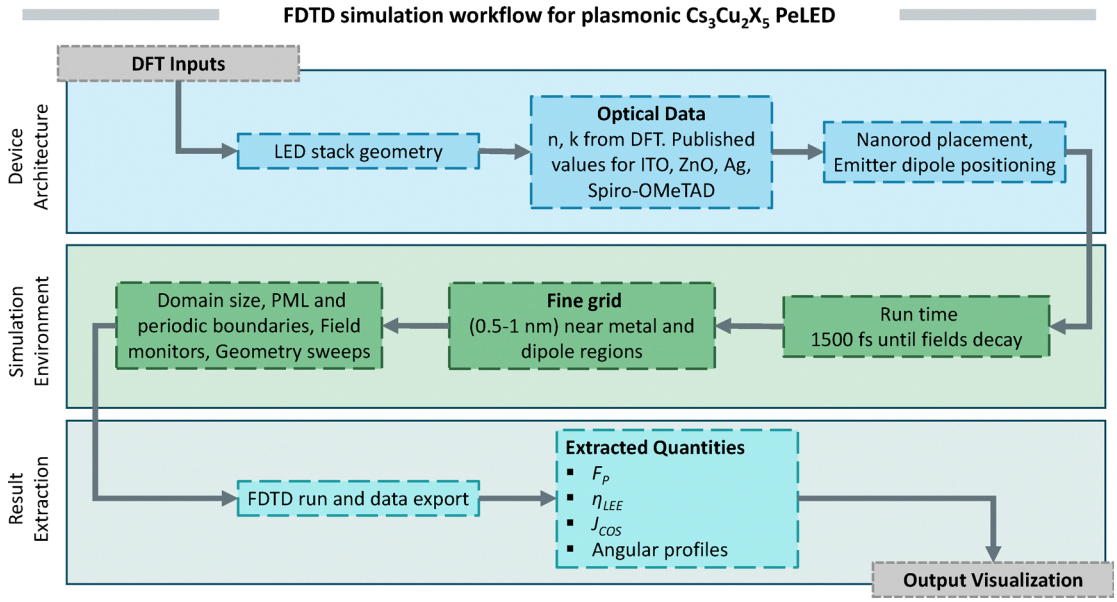

Fig. 2 Overview of the DFT-FDTD modeling approach adopted in this work. Optical constants from first-principles calculations feed into device-level electromagnetic simulations that extract key performance metrics.

mode through aspect-ratio control, making them suitable for targeting specific emission wavelengths. Nanospheres, in contrast, have a fixed dipolar resonance governed primarily by particle size and the surrounding dielectric environment. We evaluated both geometries for each $Cs_3Cu_2X_5$ variant and selected the structure with superior spectral alignment (Fig. 3).

The coupling between the plasmonic nanostructure and the emitter is modeled through near-field interaction between the dipole source and the localized surface plasmon resonance (LSPR). This interaction modifies the local density of optical states (LDOS), leading to enhanced spontaneous emission rates (Purcell effect). The strength of this coupling depends on both spatial proximity and spectral alignment. Therefore, the nanostructure geometry and dimensions are optimized to maximize overlap with the emission spectrum of each $Cs_3Cu_2X_5$ composition while maintaining an optimal emitter–plasmon separation to balance radiative enhancement and non-radiative quenching.

We positioned all nanostructures near the ZnO/perovskite interface (Fig. 4) with a core–shell architecture. We fixed the SiO_2 shell thickness at 5 nm to position the emitter within the strong near-field enhancement regime while avoiding non-radiative energy transfer to the metal, which dominates below approximately 4 nm and leads to net quenching.[57] The shell also serves as a passivation layer to prevent charge carrier quenching. We used the Palik dataset for the frequency-dependent dielectric function of silver.[53]

We optimized nanorod dimensions through parametric sweeps, varying the diameter from 8 to 25 nm and the length from 30 to 70 nm. We swept the nanosphere radius similarly to identify optimal coupling conditions. The optimization target was maximum spectral overlap between the LSPR and the composition-dependent emission peak of each $Cs_3Cu_2X_5$ variant.

2.4 Compositional analysis strategy

We ran systematic simulations across the $Cs_3Cu_2X_5$ (X = Cl, Br, I) compositional series, both with and without the plasmonic nanostructure. For each halide composition, we used the corresponding DFT-derived n and k spectra in the FDTD model.

This dual-simulation approach isolates the influence of halide-induced optical dispersion changes from plasmonic coupling effects.[62] We normalized all extracted optical parameters to their non-plasmonic counterparts to determine the enhancement introduced by the nanostructure for each composition.

From the computed field data, we extracted the Purcell factor, light extraction efficiency, near-field intensity distributions, and far-field angular patterns.

2.5 Performance metrics

Purcell factor. The Purcell factor (F_P) quantifies the enhancement of the spontaneous emission rate when an emitter is placed in a modified photonic environment compared to free space.[55] It arises from changes in the local density of optical states (LDOS) experienced by the dipole emitter. In FDTD simulations, F_P is calculated as the ratio of total power radiated by the dipole in the device structure (P_{cav}) to that in a homogeneous reference medium of equivalent refractive index (P_0)[50]

$$F_P = \frac{P_{cav}}{P_0} \quad (1)$$

This approach is valid because the emission rate is proportional to the LDOS, and the LDOS is proportional to the power emitted by the source. Values greater than unity indicate enhanced radiative recombination. Plasmonic nanostructures can produce large Purcell factors by concentrating electromagnetic fields near the emitter.[63]

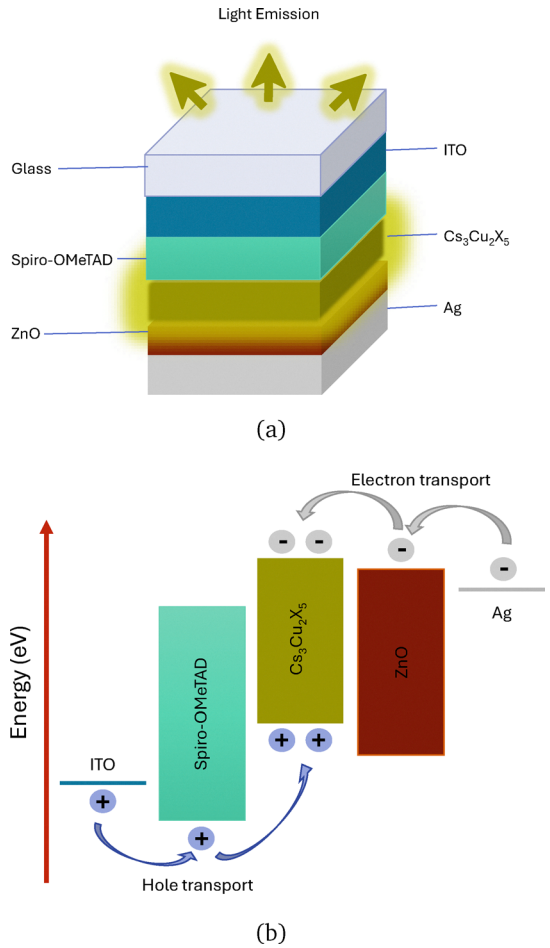

Fig. 3 (a) Schematic of the simulated PeLED stack. (b) Energy band alignment showing hole injection from ITO through Spiro-OMeTAD and electron injection from Ag through ZnO into the perovskite active layer.

LEE. The LEE represents the fraction of emitted photons that escape the device into the far field rather than being trapped by waveguide modes, substrate absorption, or total internal reflection.[64] In accordance with standard optoelectronic theory, LEE is defined as:

$$\eta_{\mathrm{LEE}} = \frac{P_{\mathrm{out}}}{P_{\mathrm{total}}} \tag{2}$$

where P_{out} is the power radiated into the upper hemisphere and P_{total} is the total power emitted by the dipole source.[64] In FDTD simulations, P_{out} is calculated by integrating the Poynting vector over a far-field monitor placed above the device structure. High refractive index contrast at layer interfaces typically limits LEE in perovskite devices to below 20% without optical engineering.[12,14] By modifying the local density of optical states (LDOS), plasmonic structures can redirect trapped modes into propagating radiation, thereby improving outcoupling.[12,64] The LEE enhancement factor is defined as the ratio of LEE with and without the plasmonic nanostructure.

Spectral overlap. Efficient plasmon-emitter coupling requires spectral alignment between the emitter photoluminescence and the LSPR of the nanostructure. The degree of overlap determines the strength of near-field interaction and the magnitude of Purcell enhancement. To quantify spectral matching independent of amplitude, the cosine similarity metric ($J_{\cos}$) is employed:[65,66]

$$J_{\cos} = \frac{\int S(\lambda), C(\lambda), \mathrm{d}\lambda}{\sqrt{\int S^2(\lambda), \mathrm{d}\lambda}\sqrt{\int C^2(\lambda), \mathrm{d}\lambda}} \tag{3}$$

where $S(\lambda)$ is the normalized emission spectrum and $C(\lambda)$ is the normalized plasmonic scattering cross-section spectrum. This metric, rooted in the Cauchy–Schwarz inequality, provides a rigorous, amplitude-independent measure of resonance alignment between the electronic transitions and the localized plasmonic modes. A value of $J_{\cos} = 1$ indicates perfect spectral alignment and $J_{\cos} = 0$ indicates no overlap.

Far-field radiation pattern. The far-field angular distribution describes the directional characteristics of light emitted from the device.[67] It is computed by projecting the near-field data to the far-field regime through standard electromagnetic transformations involving Fourier transformation of the tangential electric field components recorded at the detection surface.[68] Directional emission concentrated within a narrow angular cone improves practical light collection and utilization. Plasmonic and cavity effects can reshape the far-field pattern, concentrating emission toward the surface normal.[69]

3 Results and discussion

3.1 Electrical and optical properties of $Cs_3Cu_2X_5$

Fig. 5 presents the calculated electronic band structures and total density of states (DOS) of the $Cs_3Cu_2X_5$ (X = Cl, Br, I) compounds. The band dispersions are plotted along the high-symmetry directions of the Brillouin zone, with the Fermi level aligned at 0 eV. All three materials exhibit semiconducting behavior with direct band gaps, where both the valence band maximum (VBM) and conduction band minimum (CBM) occur at the same k-point.

For $Cs_3Cu_2Cl_5$ (Fig. 5a), a direct band gap of 2.42 eV is obtained. Upon substitution of Cl with Br (Fig. 5b), the band gap decreases to 2.15 eV, while for $Cs_3Cu_2I_5$ (Fig. 5c), the gap slightly increases to 2.34 eV. This non-monotonic trend reflects the competing effects of halogen atomic size and orbital energies. Importantly, the direct nature of the band gap is preserved across the entire halide series. Spin–orbit coupling (SOC) was included in the calculations; however, the spin-up and spin-down channels remain symmetric, indicating the absence of spin polarization in these systems.

The valence bands near the VBM are relatively flat, indicating localized electronic states primarily arising from strong Cu–X orbital hybridization. In particular, the projected density of states (PDOS) shown in Fig. 5(d–f) reveals that the valence band region is dominated by halogen p-states with significant contributions from Cu d-orbitals, confirming pronounced Cu–X hybridization. In contrast, the conduction bands exhibit greater dispersion, suggesting comparatively higher carrier mobility for electrons, and are mainly composed of Cu d-states with minor contributions from Cs orbitals. The corresponding total DOS

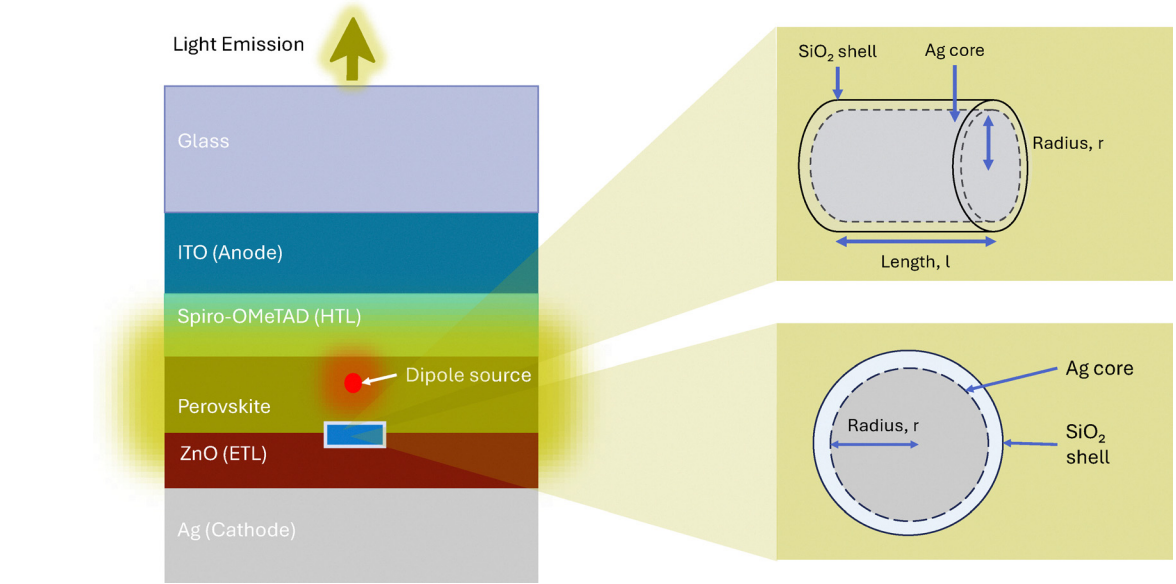

Fig. 4 Placement of the dipole source and plasmonic nanostructures within the LED stack. A core–shell Ag/SiO_2 nanorod (variable radius 8–25 nm, length 30–70 nm) is used for $Cs_3Cu_2Cl_5$ and $Cs_3Cu_2Br_5$, while a nanosphere geometry is employed for $Cs_3Cu_2I_5$. The 5 nm SiO_2 shell prevents non-radiative quenching while maintaining near-field coupling.

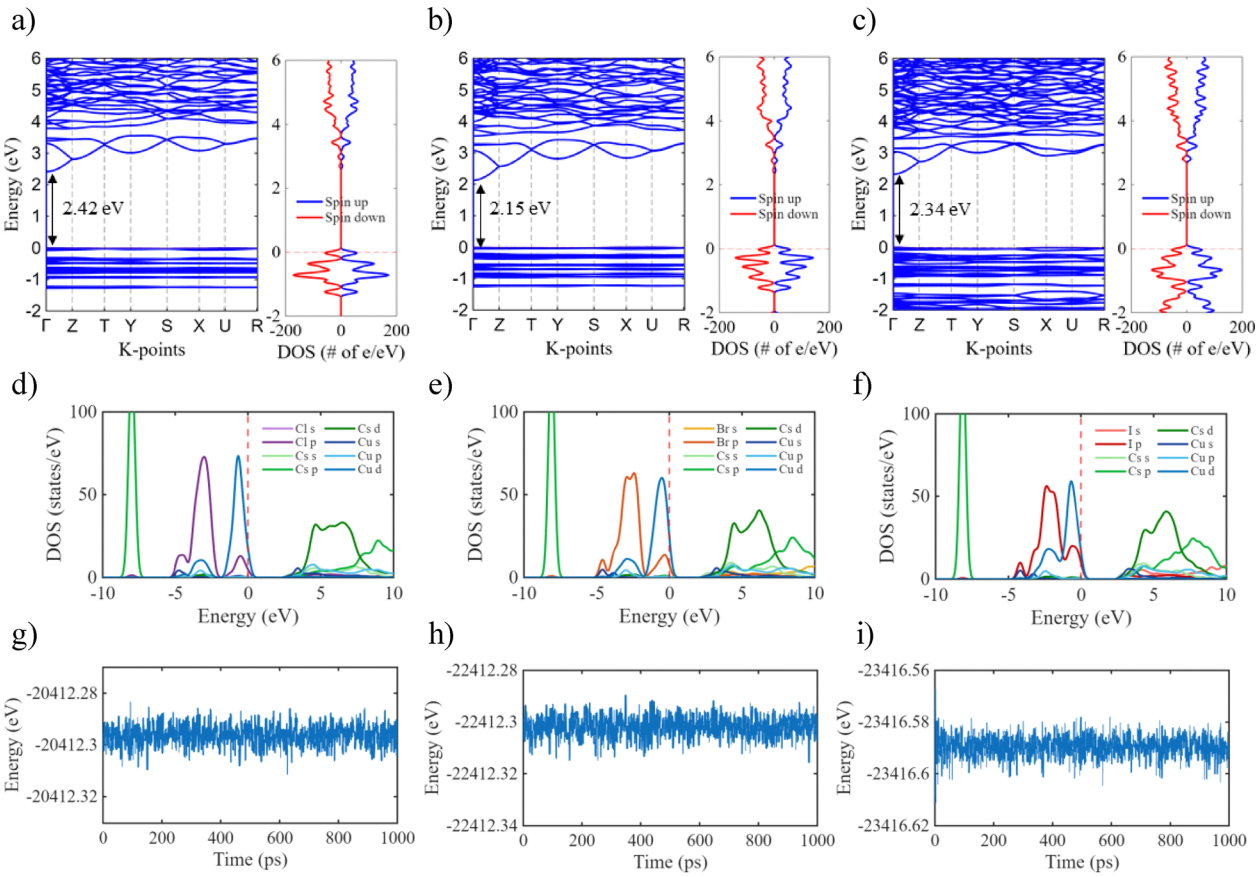

Fig. 5 Calculated electronic band structures, total and projected density of states (DOS), and thermal stability of $Cs_3Cu_2X_5$ compounds. (a)–(c) show the electronic band structures and corresponding total DOS of $Cs_3Cu_2Cl_5$, $Cs_3Cu_2Br_5$, and $Cs_3Cu_2I_5$, respectively, plotted along high-symmetry directions of the Brillouin zone, with the Fermi level set at 0 eV (red dashed line). All compounds exhibit direct band gaps of 2.42 eV, 2.15 eV, and 2.34 eV, respectively. (d)–(f) present the orbital-resolved projected DOS, indicating that the valence band is mainly dominated by halogen p-states with noticeable hybridization from Cu d-orbitals, while the conduction band is primarily governed by Cu d-states with minor contributions from Cs orbitals. (g)–(i) show the time evolution of total energy from molecular dynamics simulations at 298 K with the NVT ensemble, where the small energy fluctuations confirm the thermal stability of the compounds under ambient conditions.

plots (right panels of Fig. 5) further confirm the semiconducting nature, showing well-defined band gaps without any mid-gap states.

To evaluate thermal stability under realistic conditions, molecular dynamics (MD) simulations were performed in the NVT ensemble at 298 K using a Nosé–Hoover thermostat, as shown in Fig. 5g–i. The total energy exhibits only small fluctuations around equilibrium throughout the simulation time, with no noticeable drift, confirming that all three compounds remain structurally stable under ambient conditions.

Table 1 lists the optimized lattice parameters and band gaps. Calculated values for $Cs_3Cu_2Cl_5$ (a = 9.57 Å, b = 10.74 Å, c = 13.41 Å, E_g = 2.42 eV) match well with experiments and earlier experimental and theoretical works. $Cs_3Cu_2Br_5$ comes out at a = 9.90 Å, b = 11.16 Å, c = 13.93 Å with a 2.15 eV gap. $Cs_3Cu_2I_5$ has a = 10.46 Å, b = 11.89 Å, c = 14.70 Å and a 2.34 eV gap, again matching the literature. The thermodynamic stability of the compounds is further evaluated through the formation energy, calculated using

$$E_f = \frac{E_{tot}(Cs_3Cu_2X_5) - E_s(Cs) - E_s(Cu) - E_s(X)}{N}, \quad (X = Cl, Br, I) \tag{4}$$

where E_{tot} is the total energy of the compound, E_s represents the energy of the elemental reference phases, and N is the number of atoms in the unit cell. The calculated formation energies are found to be −3.278, −3.031, and −2.721 eV for $Cs_3Cu_2Cl_5$, $Cs_3Cu_2Br_5$, and $Cs_3Cu_2I_5$, respectively. The negative values confirm the thermodynamic stability of these materials. Moreover, the results are in good agreement with previously reported theoretical values, while slight deviations from experimental estimates can be attributed to differences in reference states and synthesis conditions.

The lattice expands from Cl to Br to I as the halide ions get larger in size. Longer Cu–X bonds change the orbital overlap and shift the band gaps across the series. Overall, the structural and electronic properties obtained in this work demonstrate strong consistency with experimental and previously reported DFT results, confirming the reliability of the computational methodology employed. The optical absorption coefficient is fundamentally linked to the complex dielectric function, expressed as $\varepsilon = \varepsilon_1 + i\varepsilon_2$. The imaginary component, ε_2, can be determined by examining interband transitions within the electronic band structure, yielding the following relation[70]:

$$\varepsilon_2(q \to 0_{\hat{u}}, \hbar\omega) = \frac{2e^2\pi}{\Omega\varepsilon_0}\sum_{k,v,c}\left|\langle \Psi_k^c|\mathbf{u}\cdot\mathbf{r}|\Psi_k^v\rangle\right|^2\delta\left(E_k^c - E_k^v - \hbar\omega\right) \tag{5}$$

In this expression, $\mathbf{u}$ represents the polarization vector of the incident light, e is the elementary charge, and $\hbar$ denotes the reduced Planck constant. The term $\langle \Psi_k^c|\mathbf{u}\cdot\mathbf{r}|\Psi_k^v\rangle$ corresponds to the transition matrix element utilizing the momentum operator $\mathbf{u}\cdot\mathbf{r}$. Furthermore, E_k^c and E_k^v designate the energy levels of the conduction and valence bands, respectively, at a given wave vector k, while ω is the angular frequency.

To evaluate the real component of the dielectric function, ε_1, the Kramers–Kronig relation is applied[70]:

$$\varepsilon_1(\omega) = 1 + \frac{2}{\pi}P\int_0^\infty \frac{\varepsilon_2(\omega^*)\omega^*}{\omega^{*2} - \omega^2}d\omega^* \tag{6}$$

where P indicates the Cauchy principal value of the integral.

Based on these dielectric components, the material's optical absorption coefficient, α, can be computed using the following equation:[71,72]

$$\alpha(\omega) = \frac{4\pi k(\omega)}{\lambda} = \frac{\omega\varepsilon_2(\omega)}{n(\omega)c} \tag{7}$$

where c is the speed of light under vacuum. Finally, the frequency-dependent refractive index, $n(\omega)$, and extinction coefficient, $k(\omega)$, are directly derived from the real and imaginary parts of the dielectric function *via* the following expressions[71]:

$$n(\omega) = \frac{1}{\sqrt{2}}\left[\sqrt{\varepsilon_1^2(\omega) + \varepsilon_2^2(\omega)} + \varepsilon_1(\omega)\right]^{1/2} \tag{8}$$

$$k(\omega) = \frac{1}{\sqrt{2}}\left[\sqrt{\varepsilon_1^2(\omega) + \varepsilon_2^2(\omega)} - \varepsilon_1(\omega)\right]^{1/2} \tag{9}$$

The calculated optical properties of $Cs_3Cu_2X_5$ (X = Cl, Br, I) are illustrated in Fig. 6, including the real part of the refractive index (n), extinction coefficient (k), and absorption coefficient as functions of photon energy in the range of 0–20 eV.

Fig. 6(a) presents the real part of the refractive index (n). In the low-energy region, all compounds exhibit relatively high static refractive indices, indicating a strong polarization response. Prominent peaks in n are observed in the ultraviolet (UV) region, which originate from interband electronic transitions. Among the three compounds, noticeable variations in peak positions and magnitudes are observed, reflecting the influence of halogen substitution on the electronic polarizability and band structure.

The extinction coefficient (k), shown in Fig. 6(b), remains nearly zero in the low-energy region below the band gap, confirming the semiconducting nature of these materials. As the photon energy exceeds the band gap, k increases sharply due to the onset of interband transitions. Distinct peaks appear in the UV region, corresponding to strong optical transitions between the valence and conduction bands. The halogen-dependent shift

Table 1 Lattice parameters in the a, b, and c directions, band gaps E_g, and formation energies E_f of the $Cs_3Cu_2X_5$ materials

Material	a (Å)	b (Å)	c (Å)	E_g (eV)	E_f (eV)	Remarks
$Cs_3Cu_2Cl_5$	9.57	10.74	13.41	2.42	−3.278	This work
	9.18	10.51	13.14	2.45	−1.565	Experimental[58]
	9.60	10.79	13.59	2.34	−3.396	DFT[59]
$Cs_3Cu_2Br_5$	9.90	11.16	13.93	2.15	−3.031	This work
	9.58	10.98	13.63	2.25	−1.384	Experimental[60]
	9.92	11.19	13.92	2.09	−3.129	DFT[59]
$Cs_3Cu_2I_5$	10.46	11.89	14.70	2.34	−2.721	This work
	10.22	11.66	14.40	2.44	−1.106	Experimental[61]
	10.50	11.89	14.78	2.29	−2.855	DFT[59]

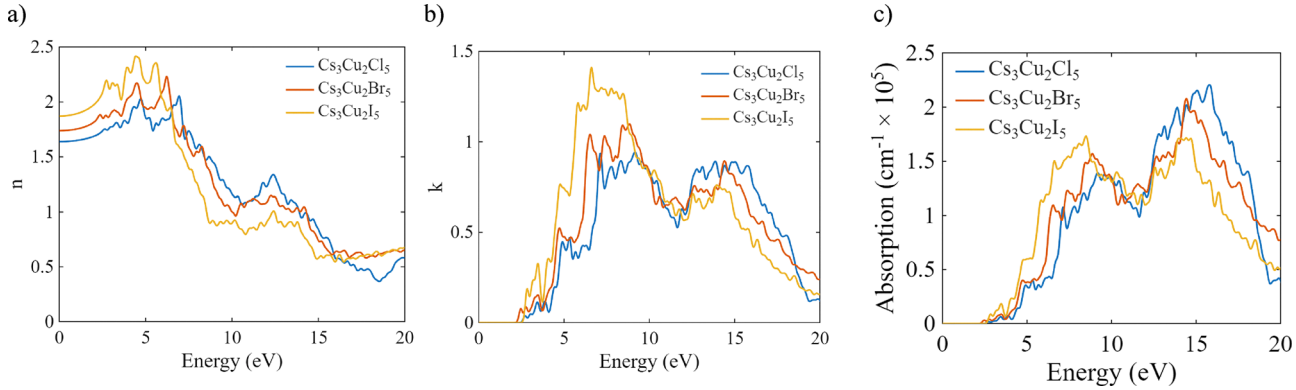

Fig. 6 Optical properties of $Cs_3Cu_2X_5$ (X = Cl, Br, I): (a) *n*, (b) *k*, and (c) absorption coefficient as a function of photon energy. The calculated spectra are presented in the energy range of 0–20 eV for $Cs_3Cu_2Cl_5$, $Cs_3Cu_2Br_5$, and $Cs_3Cu_2I_5$. The absorption coefficient is expressed in cm^{-1} (scaled by 10^5). The distinct peak structures in *n*, *k*, and absorption originate from interband electronic transitions, reflecting the influence of halogen substitution on the optical response of the compounds.

in peak positions further demonstrates the tunability of the optical response through chemical substitution. The prominent peaks observed in the refractive index (n) and extinction coefficient (k) spectra (Fig. 6) are fundamentally rooted in the material's electronic structure. These features represent strong interband electronic transitions between the localized Cu-3d orbitals in the bi-octahedral dimers and the conduction band states. The halogen-dependent shift in these peaks reflects changes in electronic polarizability as the Cu–X bond length increases across the Cl–Br–I series.

Fig. 6(c) shows how absorption varies with photon energy. The absorption edge lines up with the band gap for each compound, as expected from the electronic structure. All three absorb strongly in the UV with peaks around 10^5 cm^{-1}. The differences between $Cs_3Cu_2Cl_5$, $Cs_3Cu_2Br_5$, and $Cs_3Cu_2I_5$ come from how the orbitals mix and how the bands disperse when you change the halogen.

The optical spectra confirm strong UV transitions across the series. Changing the halide tunes the optical response. These characteristics suggest potential applications in ultraviolet optoelectronic and photonic devices.

3.2 Composition-dependent plasmonic enhancement

Table 2 summarizes the optimized nanostructure dimensions and FDTD results for all three halides. $Cs_3Cu_2Cl_5$ achieves the highest Purcell factor (4.4×) and LEE (30%). $Cs_3Cu_2Br_5$ shows the best spectral overlap (J_{cos} = 0.955), while $Cs_3Cu_2I_5$ falls behind on both metrics. These differences are due to how the optical constants of each material interact with the plasmon resonance. The lower refractive index of the chloride system improves light extraction. The bromide system benefits from better wavelength matching with the nanorod LSPR.

$Cs_3Cu_2Cl_5$. Fig. 7 shows the device-level performance for the $Cs_3Cu_2Cl_5$-based LED. Purcell enhancement of 4.4× can be seen at 539 nm (Fig. 7a). This enhancement indicates faster spontaneous emission due to increased LDOS near the Ag nanorod surface. The relatively low refractive index of $Cs_3Cu_2Cl_5$ ($n \approx 1.9$ at 539 nm) reduces dielectric screening of the plasmonic near-field. This allows stronger coupling between the emitter dipole and the plasmon mode compared to the higher-index Br and I compositions.

The spectral overlap peaks at the same wavelength (Fig. 7b) with J_{cos} = 0.946. This confirms good resonance matching between the emitter and the nanorod LSPR. Strong spectral alignment is important because Purcell enhancement depends on overlap between the emission spectrum and plasmonic mode density.

LEE goes from around 18% without the nanorod to 30% with it (Fig. 7c), a 1.7× improvement. The plasmon scatters light that would otherwise remain trapped in the waveguide and substrate modes, redirecting it into the far field. The LEE peak appears at slightly longer wavelengths than the Purcell peak. This happens because near-field coupling and far-field scattering do not optimize at the same wavelength. Strong near-field enhancement requires tight mode confinement, while efficient extraction needs good scattering into propagating waves. These two requirements compete to some extent. Nevertheless, 30% extraction compares favorably to the 10–20% typical of perovskite LEDs without optical engineering.

The far-field pattern at 539 nm (Fig. 7d) is smooth and close to Lambertian. Most of the intensity falls within ±60 Å of normal, with no secondary lobes. This indicates that the nanorod acts as a

Table 2 FDTD results for plasmonic $Cs_3Cu_2X_5$-based PeLEDs

X	Composition	Emission λ (nm)	Nanostructure	Radius (nm)	Length (nm)	Purcell factor	Peak λ (nm)	LEE (%)	J_{cos}
Cl	$Cs_3Cu_2Cl_5$	529	Nanorod	12	50	4.4	539	30	0.946
Br	$Cs_3Cu_2Br_5$	593	Nanorod	18	50	2.8	600	26	0.955
I	$Cs_3Cu_2I_5$	541	Nanosphere	15	—	2.4	538	10	0.846

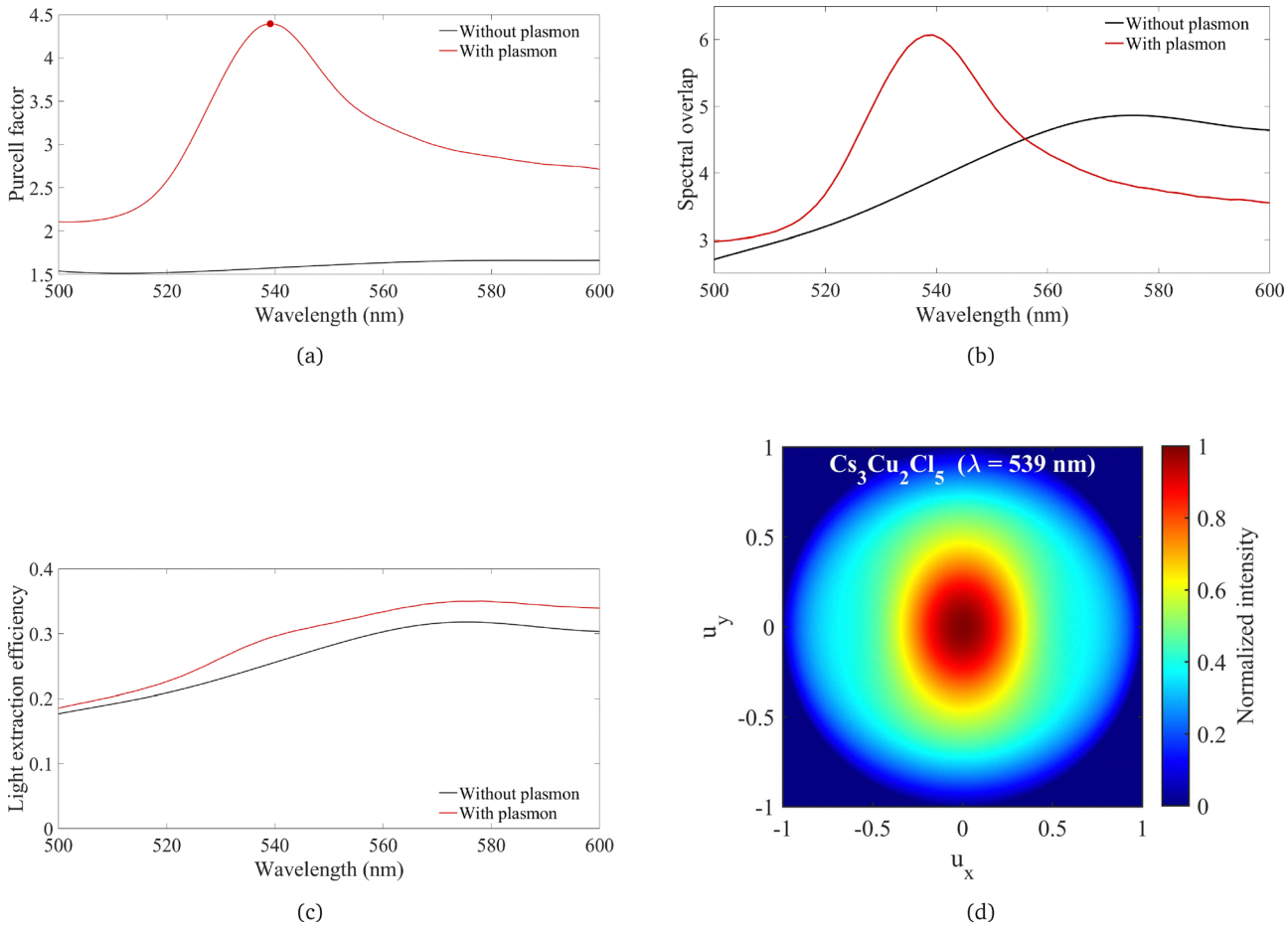

Fig. 7 Device-level optical performance of the $Cs_3Cu_2Cl_5$-based LED with optimized Ag/SiO_2 nanorods. (a) Purcell factor. (b) Spectral overlap. (c) Light extraction efficiency. (d) Far-field radiation pattern at 539 nm.

scattering center rather than an antenna with narrow directionality. Wide-angle emission like this is desirable for display applications where uniform brightness across viewing angles is important.

$Cs_3Cu_2Br_5$. The $Cs_3Cu_2Br_5$-based LED shows 2.8× Purcell enhancement at 600 nm (Fig. 8a). This is lower than that of $Cs_3Cu_2Cl_5$ even though the spectral overlap is the highest among all three compositions (J_{cos} = 0.955, Fig. 8b). This can be explained by the higher refractive index of $Cs_3Cu_2Br_5$ ($n \approx 2.1$ at 600 nm). A higher index increases dielectric screening around the nanorod and reduces the effective near-field intensity at the emitter location. The Purcell factor scales roughly as $F_P \propto n^{-3}$, which explains the reduced enhancement in higher-index materials.

LEE improves from around 20% to 26% (Fig. 8c). This 1.3× enhancement is more modest than for $Cs_3Cu_2Cl_5$. The higher refractive index increases the critical angle for total internal reflection. As a result, more photons remain trapped in substrate and waveguide modes. The extinction coefficient of $Cs_3Cu_2Br_5$ is also higher at the emission wavelength (Fig. 8b), leading to increased reabsorption losses.

The far-field pattern at 600 nm (Fig. 8d) is broader than that of $Cs_3Cu_2Cl_5$. More intensity appears at oblique angles. This broadening suggests that some emitted light couples to guided modes before being scattered out. The longer optical path associated with these guided modes also contributes to lower LEE.

$Cs_3Cu_2I_5$. For $Cs_3Cu_2I_5$, a nanosphere geometry was used instead of a nanorod. Parametric optimization showed that nanorods could not achieve good spectral overlap with the $Cs_3Cu_2I_5$ emission at 541 nm. The different dielectric environment created by the iodide composition shifts the optimal LSPR condition. The isotropic field distribution of the nanospheres provides better mode matching with the emission dipole orientation in this material.

The Purcell factor peaks at 2.4× at 538 nm (Fig. 9a). This is the lowest among the three compositions. Without plasmonic coupling, the Purcell factor stays near 1.1 to 1.2×. This indicates weak cavity effects in the device stack at this emission wavelength. The spectral overlap is also the lowest (J_{cos} = 0.846, Fig. 9b). This reflects limited alignment between the nanosphere LSPR and the emission spectrum.

LEE remains at only 10% (Fig. 9c). This is much lower than the Cl and Br compositions. The combination of high refractive index ($n \approx 2.2$) and substantial extinction coefficient at the emission wavelength promotes strong optical confinement and reabsorption. The far-field pattern (Fig. 9d) shows clear distortion

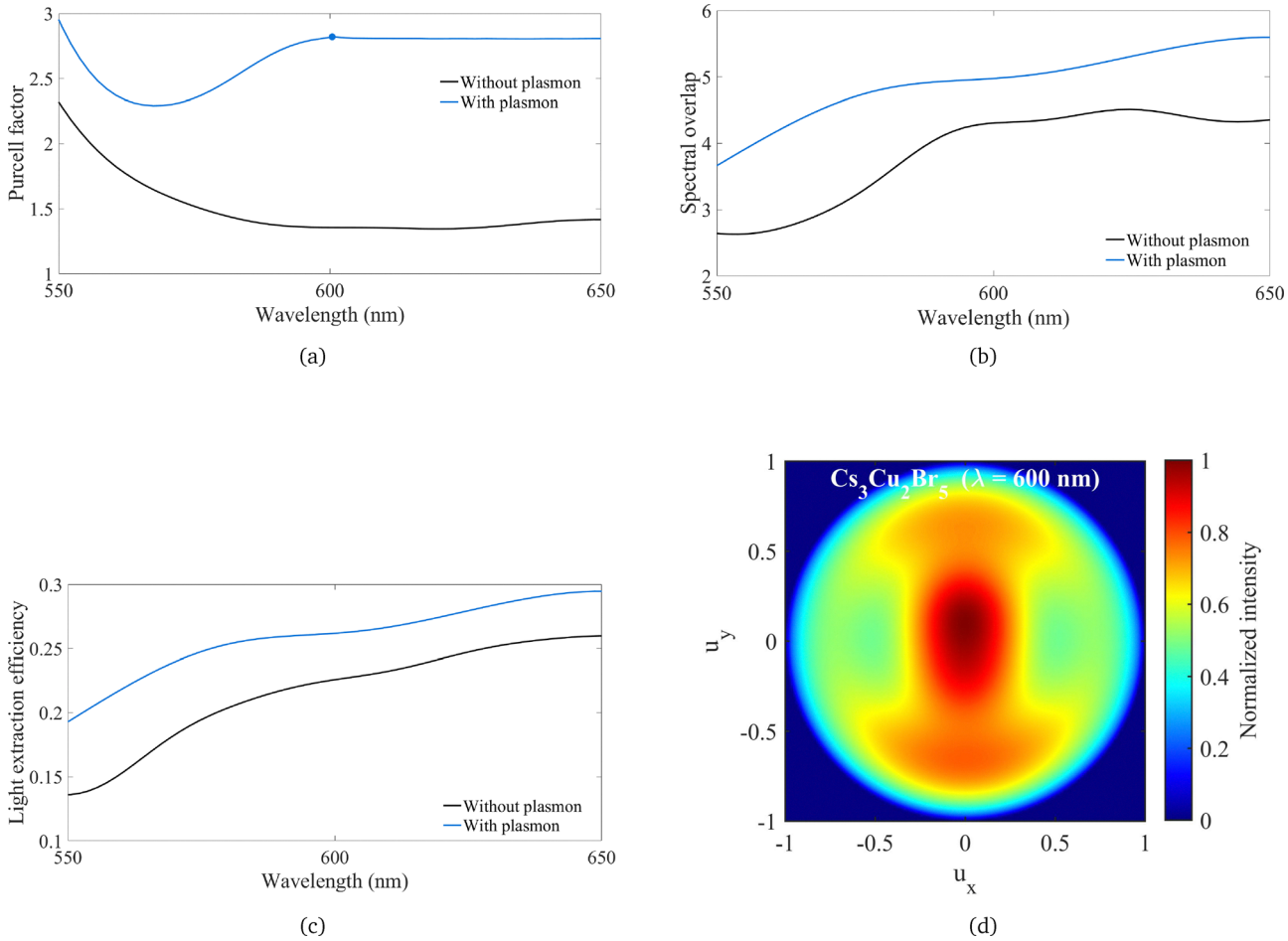

Fig. 8 Device-level optical performance of the $Cs_3Cu_2Br_5$-based LED with optimized Ag/SiO_2 nanorods. (a) Purcell factor. (b) Spectral overlap. (c) Light extraction efficiency. (d) Far-field radiation pattern at 600 nm.

with significant intensity at high angles. This confirms that many emitted photons couple to guided or substrate modes rather than escaping to free space.

The $Cs_3Cu_2I_5$ case shows a key limitation. Even with reasonable Purcell enhancement, extraction remains poor. Accelerating emission does not guarantee that photons escape the device. The n and k of the material set an upper bound on extraction. Plasmonic enhancement cannot fully compensate for a high-index environment.

3.3 Comparative performance and trade-off analysis

Fig. 10 compares all three halide compositions. The differences in plasmonic enhancement across the halide series are directly connected to the DFT-derived optical constants. Examining them together helps explain why some halides respond better than others. The integration of metallic nanostructures fundamentally impacts the optical performance by modifying the local density of optical states (LDOS). This modification facilitates the Purcell effect, accelerating the spontaneous emission rate and redirecting evanescent modes into propagating far-field radiation. The scientific reason for the superior performance of $Cs_3Cu_2Cl_5$ is its lower refractive index ($n \approx 1.9$), which minimizes dielectric screening of the plasmonic near-field. In contrast, the higher refractive index of $Cs_3Cu_2I_5$ ($n \approx 2.2$) leads to stronger screening and increased optical confinement, fundamentally limiting the outcoupling potential regardless of the Purcell enhancement.

Peak enhancement comparison. Fig. 10(a) plots the peak enhancement values for each halide. $Cs_3Cu_2Cl_5$ leads with a 4.4× Purcell factor, 30% LEE, and 0.946 spectral overlap. The chloride performs well because its refractive index is low ($n \approx 1.9$). This reduces dielectric screening and allows the emitter to couple more strongly to the nanorod near-field. The plasmonic field penetrates further into the active layer before being damped. $Cs_3Cu_2Br_5$ and $Cs_3Cu_2I_5$ have higher refractive indices. As a result, nanostructure geometry produces weaker enhancement in these materials.

$Cs_3Cu_2Br_5$ exhibits moderate but balanced enhancement across all metrics. The higher refractive index ($n \approx 2.1$) limits the Purcell factor to 2.8× despite achieving the best spectral overlap (0.955). This shows that spectral matching alone cannot compensate for increased dielectric losses in higher-index materials.

$Cs_3Cu_2I_5$ shows the weakest response with a Purcell factor of 2.4× and LEE of only 10%. The high refractive index ($n \approx 2.2$) and large extinction coefficient at the emission wavelength cause strong optical confinement. Even with a nanosphere

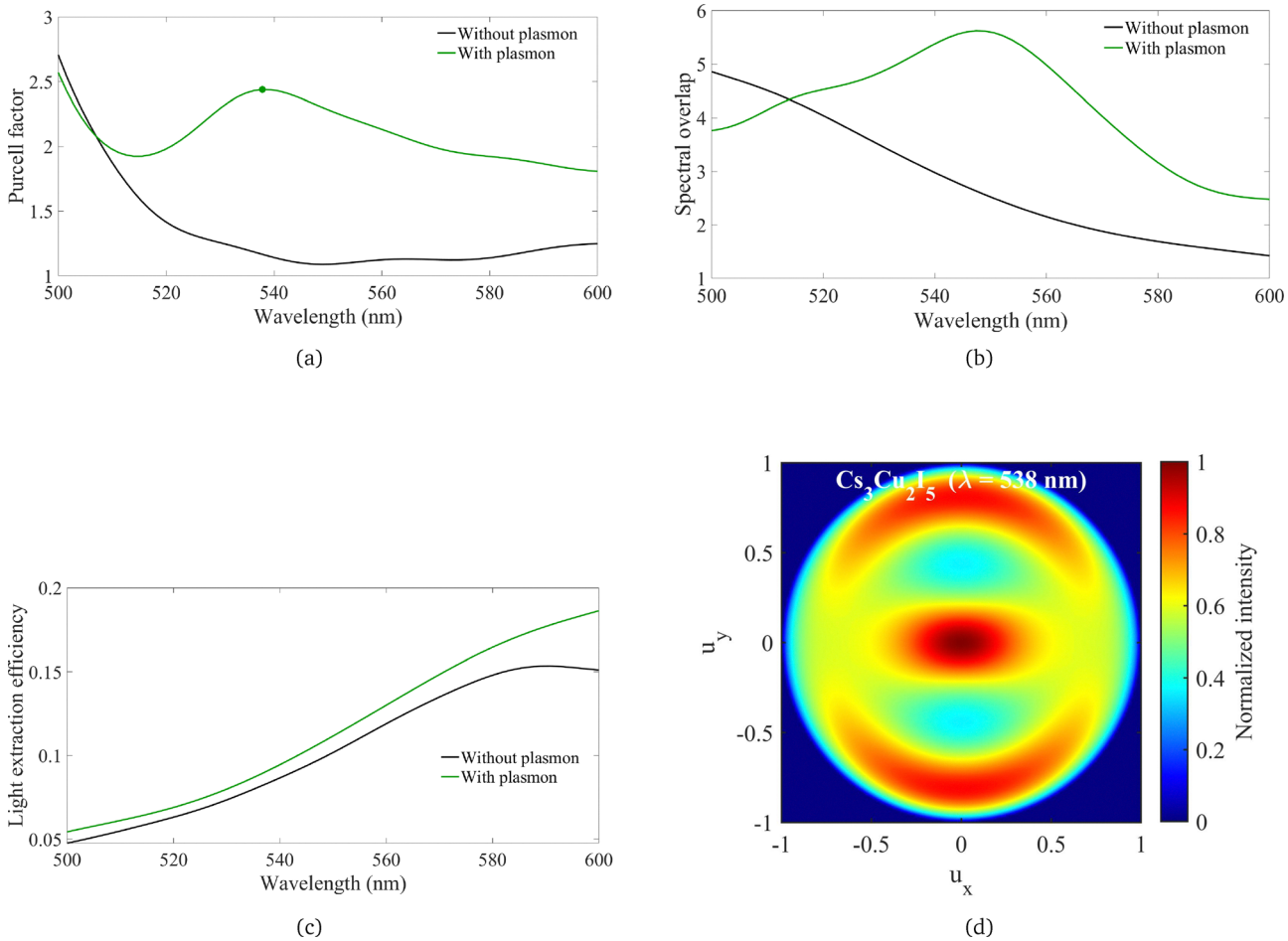

Fig. 9 Device-level optical performance of the $Cs_3Cu_2I_5$-based LED with optimized Ag/SiO_2 nanospheres. (a) Purcell factor. (b) Spectral overlap. (c) Light extraction efficiency. (d) Far-field radiation pattern at 538 nm.

geometry optimized for this composition, the spectral overlap remains limited at 0.846.

Purcell factor and LEE trade-off. Fig. 10(b) maps the relationship between peak Purcell factor and peak LEE. The shaded regions represent the accessible design space for each composition through nanostructure geometry optimization.

$Cs_3Cu_2Cl_5$ occupies the upper-right region where both high Purcell factor and high LEE are achievable. This is because the low refractive index creates favourable conditions for both near-field enhancement and far-field extraction. The plasmonic near-field is less screened, and the critical angle for total internal reflection is larger. Both effects work together to improve device performance.

$Cs_3Cu_2Br_5$ lies in an intermediate region. The higher index material can still achieve reasonable Purcell enhancement through geometry optimization. However, the increased optical confinement limits how much of this enhanced emission can be extracted to the far field.

$Cs_3Cu_2I_5$ sits in the lower-left region. The high refractive index creates a fundamental trade-off. Stronger near-field confinement could increase the Purcell factor, but this same confinement traps more light inside the device. As a result, the design space is limited by the intrinsic optical properties of the material rather than by the plasmonic structure.

This points out a key design consideration. For plasmon-enhanced LEDs, the choice of emitter material matters as much as the nanostructure geometry. A high Purcell factor in a high-index host may not necessarily improve device output efficiency when most of the generated photons are trapped inside the device.

Multi-parameter summary. Fig. 10(c) shows a normalized radar plot covering five performance metrics.

$Cs_3Cu_2Cl_5$ covers the largest area, with the highest values for LEE, Purcell factor, and radiated power. However, its spectral overlap is slightly lower than that of $Cs_3Cu_2Br_5$. The overall balanced shape indicates that plasmonic enhancement and light extraction work well together in this low-index material.

$Cs_3Cu_2Br_5$ shows the best spectral overlap among the three materials. But the other metrics are moderate, resulting in a smaller balanced profile. The good wavelength matching with the nanorod LSPR explains the strong overlap despite the higher refractive index.

$Cs_3Cu_2I_5$ has the smallest area overall. LEE and radiated power are low, while spectral overlap remains comparable to

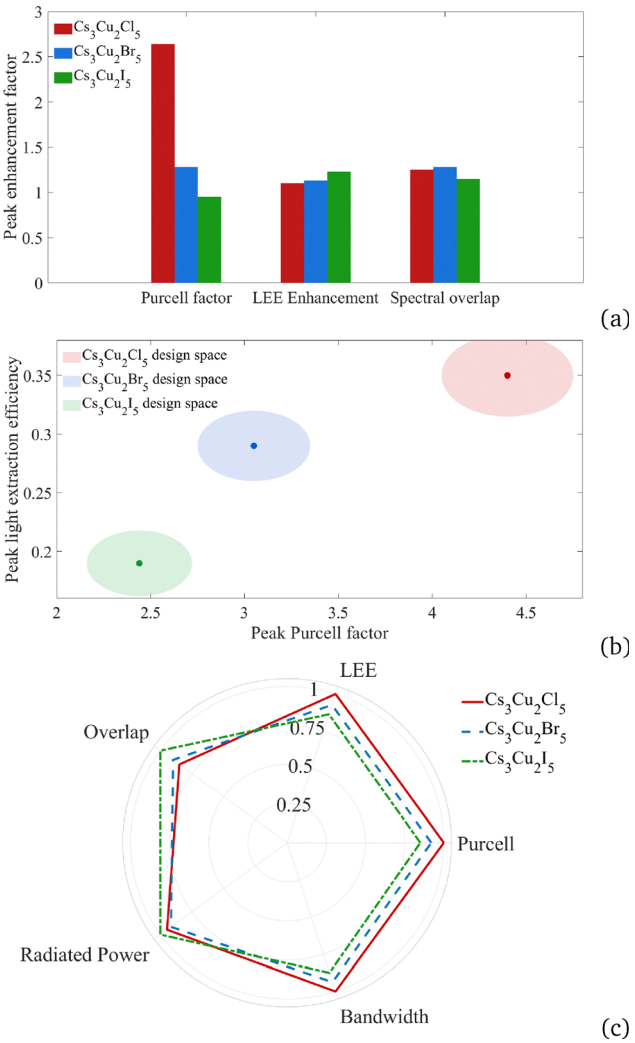

Fig. 10 Comparative performance of plasmon-enhanced $Cs_3Cu_2X_5$-based LEDs. (a) Peak enhancement factors for Purcell factor, LEE, and spectral overlap. (b) Purcell factor and LEE trade-off map showing the design space for each composition. (c) Radar plot comparing normalized performance metrics across the halide series.

the other two. This confirms that light confinement limits $Cs_3Cu_2I_5$ more than the other two materials.

Among the $Cs_3Cu_2X_5$ series, $Cs_3Cu_2Cl_5$ is the most promising candidate for plasmon-enhanced LEDs. Low refractive index and strong plasmonic coupling of $Cs_3Cu_2Cl_5$ pave the way for improved device efficiency.

3.4 Dependence of radiated power on wavelength and emitter–plasmon distance

Radiated power is mapped against wavelength and emitter–plasmon distance. This helps visualize how near-field coupling converts into usable light output. The mapping also explains why a 5 nm SiO_2 shell gives the best performance. Fig. 11 and 12 present the results for $Cs_3Cu_2Cl_5$ and $Cs_3Cu_2Br_5$, respectively. Each figure includes a 3D surface plot that shows the overall trend and a 2D contour map that highlights the optimal operating region.

$Cs_3Cu_2Cl_5$. Fig. 11 shows the radiated power distribution for $Cs_3Cu_2Cl_5$. A maximum occurs at around 530 to 540 nm wavelength and 15 nm emitter-plasmon separation. The sharp peak in Fig. 11(a) shows that efficient near-field to far-field conversion only happens within a narrow distance window.

This behavior results from two competing effects. At short distances below 10 nm, the emitter couples strongly to the plasmonic near-field. But this strong coupling also opens non-radiative decay channels. Energy transfers to the metal and dissipates as heat in the Ag core instead of radiating to the far field. At longer distances above 20 nm, the near-field intensity drops off exponentially. Coupling becomes too weak to provide meaningful enhancement.

The optimal distance of around 15 nm balances these competing effects. At this separation, the emitter experiences strong field enhancement while staying outside the dominant quenching zone. The contour plot in Fig. 11(b) shows a bright horizontal band at this distance across the 520 to 560 nm wavelength range. The narrow spectral width of this band shows the resonant nature of plasmonic enhancement. Maximum radiation occurs when the emission wavelength matches both the LSPR and the optimal coupling distance.

The 5 nm SiO_2 shell thickness used in this work places the perovskite emitter layer at approximately 10 to 20 nm from the Ag core surface, depending on dipole position within the active layer. This range falls within the optimal coupling window identified in Fig. 11(b), validating the shell design choice.

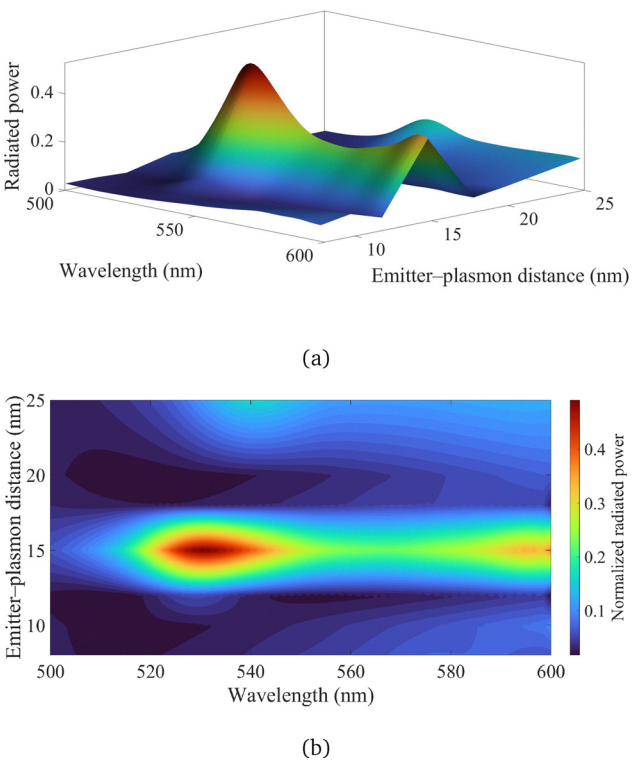

Fig. 11 Distance and wavelength dependent radiated power for the $Cs_3Cu_2Cl_5$-based LED. (a) 3D surface plot showing a localized maximum at around 15 nm separation and 530 to 540 nm wavelength. (b) 2D contour map showing the narrow optimal coupling window.

$Cs_3Cu_2Br_5$. Fig. 12 shows the radiated power distribution for $Cs_3Cu_2Br_5$. The behaviour is notably different from $Cs_3Cu_2Cl_5$. The optimal coupling region is shifted to shorter distances of 8 to 12 nm and longer wavelengths of 620 to 650 nm.

The shift to shorter optimal distance can be explained by the higher refractive index of $Cs_3Cu_2Br_5$. The plasmonic near-field decays faster in higher-index media because the field penetration depth scales inversely with refractive index. To maintain strong coupling, the emitter must be placed closer to the metal surface. However, this also increases the risk of non-radiative quenching.

A dark band shows up at 14 to 16 nm in the contour plot of Fig. 12(b). In this range, the emitter sits too far from the metal for strong plasmonic coupling, but not far enough to radiate efficiently on its own. The high refractive index still traps much of the light through total internal reflection.

A secondary enhancement region appears around 25 nm. At this distance, plasmonic coupling weakens and the emitter behaves more like a free dipole in a layered stack. Less interaction with the metal reduces non-radiative losses, allowing some light to escape through standard outcoupling rather than plasmon-mediated scattering. However, this secondary peak is broader and weaker than the primary one, indicating that plasmonic enhancement remains the more efficient extraction path.

This more complex distance dependence explains why $Cs_3Cu_2Br_5$ has lower LEE (26%) than $Cs_3Cu_2Cl_5$ (30%). The spectral overlap values are similar for both materials. However, $Cs_3Cu_2Br_5$ has a tighter optimal coupling window and stronger optical confinement. These factors make it harder to maintain efficient extraction across the full active layer.

Design implications. This distance-dependent analysis provides important guidance for device fabrication. For $Cs_3Cu_2Cl_5$, the optimal emitter-plasmon separation of around 15 nm allows some flexibility in shell thickness and emitter positioning. For $Cs_3Cu_2Br_5$, the tighter optimal window of 8 to 12 nm requires more precise control over nanostructure placement. These constraints should be considered when translating the simulation results to experimental device fabrication.

3.5 Experimental validation and fabrication outlook

The calculated emission wavelengths agree well with experimental reports. $Cs_3Cu_2Cl_5$ emits at 525–526 nm in photoluminescence measurements,[73,74] consistent with our simulations. PLQYs approaching 100% have been reported for $Cs_3Cu_2Cl_5$ and 97% for $Cs_3Cu_2I_5$ with optimized synthesis,[75,76] confirming that these materials are intrinsically efficient emitters.

Functional $Cs_3Cu_2X_5$-based LEDs have been demonstrated. Jun *et al.* reported $Cs_3Cu_2I_5$ blue LEDs with maximum luminance of 10 cd m^{-2} using thermal evaporation.[80] Liu *et al.* achieved 70 cd m^{-2} and 0.1% EQE.[81] More recent work on mixed-phase copper halide LEDs reached 0.8% EQE.[82] The Cu^+ oxidation state provides excellent ambient stability, with films maintaining optical properties for months without encapsulation.[74]

The predicted Purcell enhancement values are comparable to other plasmon-enhanced perovskite systems (Table 3). Ag nanocube arrays coupled with perovskite quantum dots achieved 3.5-fold fluorescence intensity and 4.5-fold emission rate enhancement.[77] Ag nanowire networks demonstrated up to 6-fold enhancement.[78] Au nanoparticles in PEDOT:PSS showed 3.8-fold PL improvement in blue perovskite LEDs.[79] Our predicted LEE also exceeds the 10–20% typical of standard perovskite LEDs.[12]

Ag/SiO_2 core–shell nanoparticles have been successfully integrated into perovskite solar cells. He *et al.* showed that $Ag@SiO_2$ with 5 nm shell thickness improved the PCE by 16%.[83] Wang *et al.* demonstrated $Ag@SiO_2$ nanowires achieving 18% PCE.[84] The SiO_2 shell prevents charge transfer to the metal while preserving near-field coupling.

Several fabrication challenges should be noted. Precise nanoparticle positioning within the device stack remains difficult. Solution-processed deposition may yield non-uniform distribution, reducing the average enhancement below simulated values. Nevertheless, both $Cs_3Cu_2X_5$ films and Ag/SiO_2 nanoparticles can be

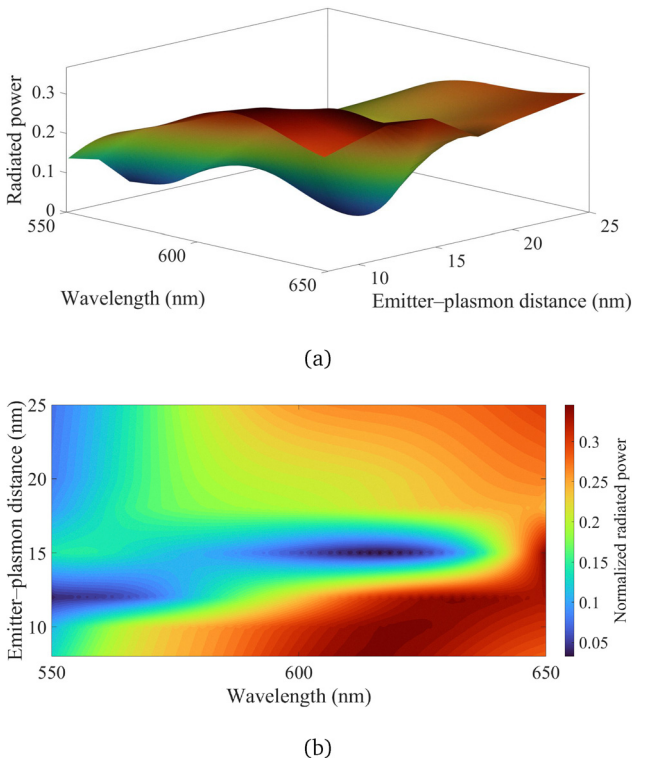

Fig. 12 Distance and wavelength dependent radiated power for the $Cs_3Cu_2Br_5$-based LED. (a) 3D surface plot showing a broader maximum compared to $Cs_3Cu_2Cl_5$. (b) 2D contour map revealing a dark band at 14 to 16 nm and secondary enhancement at around 25 nm.

Table 3 Comparison of plasmonic enhancement in perovskite light-emitting systems

Plasmonic structure	Emitter	Enhancement	Ref.
Ag nanocubes	$CsPbBr_3$ QDs	3.5× PL, 4.5× rate	77
Ag nanowire networks	$CsPbBr_3$ QDs	6× PL	78
Au NPs in PEDOT:PSS	$CsPbBr_3$	3.8× PL	79
Ag/SiO_2 nanorods	$Cs_3Cu_2Cl_5$	4.4× Purcell	This work
Ag/SiO_2 nanorods	$Cs_3Cu_2Br_5$	2.8× Purcell	This work
Ag/SiO_2 nanospheres	$Cs_3Cu_2I_5$	2.4× Purcell	This work

synthesized using established methods, suggesting that experimental realization is feasible.

Conclusions

An integrated DFT-FDTD framework has been developed to investigate plasmon-enhanced light extraction in lead-free $Cs_3Cu_2X_5$ (X = Cl, Br, I) LEDs. First-principles calculations provided composition-specific optical constants that were directly implemented in device-level FDTD simulations for nanostructure optimization.

Among the three compositions studied, $Cs_3Cu_2Cl_5$ shows the best overall performance. It achieves a 4.4× Purcell enhancement, 30% light extraction efficiency, and near-Lambertian far-field emission. This superior response is due to the lower refractive index of the material. The low index reduces dielectric screening and allows stronger near-field coupling with the plasmonic nanorod.

$Cs_3Cu_2Br_5$ has the highest spectral overlap (0.955), but the extraction efficiency is only 26%. The increased optical confinement limits light output. $Cs_3Cu_2I_5$ shows the weakest response with the extraction efficiency limited to only 10%. This shows that Purcell enhancement alone does not guarantee efficient light extraction in high-index materials.

The distance analysis reveals that optimal coupling conditions depend on the composition. $Cs_3Cu_2Cl_5$ has a wider tolerance window with best performance near 15 nm. $Cs_3Cu_2Br_5$ requires tighter control at 8–12 nm. These differences are important for experimental device fabrication.

Some limitations should be noted. The simulations assume high internal quantum efficiency. Non-radiative recombination and defect losses are not included. The reported values therefore represent the optical upper bounds. Real device performance will also depend on material quality and defect passivation. Ohmic losses in the metal nanostructures also create a trade-off between radiative enhancement and absorption. Careful spacer design is needed to manage this balance.

The results show that optical design for plasmon-enhanced lead-free LEDs needs to account for composition. The combination of chemical stability, high intrinsic quantum yield, and strong plasmonic coupling identifies $Cs_3Cu_2Cl_5$ as a promising candidate for next-generation light-emitting applications. Experimental validation through fabrication of plasmon-integrated $Cs_3Cu_2X_5$ devices represents the logical next step.

The present work is focused on optical and plasmonic properties within the DFT-FDTD framework. Thermoelectric properties of $Cs_3Cu_2X_5$ compounds, including transport coefficients and figure of merit, were not investigated here as they require a separate Boltzmann transport-based computational approach. Given the low-dimensional crystal structure and strong electron–phonon coupling in these materials, thermoelectric characterization represents a promising direction for future work.

Author contributions

Shoumik Debnath: conceptualization, methodology, software, validation, formal analysis, investigation, data curation, writing – original draft, writing – review & editing, and visualization. Sudipta Saha: DFT calculations, methodology, software, validation, writing – original draft, and writing – review & editing. Khondokar Zahin: validation and writing – review & editing. Ying Yin Tsui: editing & supervision. Md. Zahurul Islam: writing – review & supervision, and project administration.

Conflicts of interest

There are no conflicts to declare.

Data availability

Representative FDTD simulation files supporting this study are available on GitHub at https://github.com/debnath-shoumik/PeLED_FDTD_Cs3Cu2X5. All remaining data are available from the corresponding author upon reasonable request.

Acknowledgements

The authors acknowledge the financial support provided by the Basic Research Grant, Bangladesh University of Engineering and Technology (BUET), under Office Order No.: Shongstha/R-60/Re-2413, dated 10 October 2023 (Professor Dr Md. Zahurul Islam). The authors also acknowledge the logistical support provided by the Department of Electrical and Electronic Engineering (EEE), BUET, throughout the duration of this work.

References

1 L. Kong, Y. Sun, B. Zhao, K. Ji, J. Feng, J. Dong, Y. Wang, Z. Liu, S. Maqbool, Y. Li, Y. Yang, L. Dai, W. Lee, C. Cho, S. Stranks, R. Friend, N. Wang, N. Greenham and X. Yang, *Nature*, 2024, **631**, 73–79.
2 C. Li, T. Y. Huang, Y. Lai, Y. Huang and C. S. Tan, *Mater. Today Electron.*, 2024, **8**, 100095.
3 Y. Nong, J. Yao, J. Li, L. Xu, Z. Yang, C. Li and J. Song, *Adv. Mater.*, 2024, **36**, 2402325.
4 C. Cho, Y. Sun, J. You, L. Cui and N. Greenham, *Adv. Funct. Mater.*, 2024, **34**, 2411556.
5 M. Li, Y. Yang, Z. Kuang, C. Hao, S. Wang, F. Lu, Z. Liu, J. Liu, L. Zeng, Y. Cai, Y. Mao, J. Guo, H. Tian, G. Xing, Y. Cao, C. Ma, N. Wang, Q. Peng, L. Zhu, W. Huang and J. Wang, *Nature*, 2024, **630**, 631–635.
6 C. Ma, M. Ni, X. Liu, K. Zhan, M. Chen, S. Li, F. Li, H. Wang and Y. Dang, *CrystEngComm*, 2025, **27**, 3853–3876.
7 Y. Xiao, Q. Xue, X. Liu, F. Gao and G. Xie, *Innovation*, 2024, **5**, 100553.
8 D. Yang, B. Zhao, T. Yang, R. Lai, D. Lan, R. Friend and D. Di, *Adv. Funct. Mater.*, 2022, **32**, 2109495.
9 I. López-Fernández, D. Valli, C. Wang, S. Samanta, T. Okamoto, Y. Huang, K. Sun, Y. Liu, V. Chirvony, A. Patra, J. Zito, L. De Trizio, D. Gaur, H. Sun, Z. Xia, X. Li, H. Zeng, I. Mora-Seró, N. Pradhan, J. Martínez-Pastor, P. Müller-Buschbaum, V. Biju,

T. Debnath, M. Saliba, E. Debroye, R. Hoye, I. Infante, L. Manna and L. Polavarapu, *Adv. Funct. Mater.*, 2024, **34**, 2307896.
10 L. Zhang, C. Sun, T. He, Y. Jiang, J. Wei, Y. Huang and M. Yuan, *Light: Sci. Appl.*, 2021, **10**, 61.
11 J. Chen, H. Xiang, J. Wang, R. Wang, Y. Li, Q. Shan, X. Xu, Y. Dong, C. Wei and H. Zeng, *ACS Nano*, 2021, **15**, 17150–17174.
12 B. Zhao, M. Vasilopoulou, A. Fakharuddin, F. Gao, A. B. M. Yusoff, R. Friend and D. Di, *Nat. Nanotechnol.*, 2023, **18**, 981–992.
13 C. Liu, B. Li and M. Qiu, *Adv. Devices Instrum.*, 2024, **5**, 0045.
14 S. Rahimi, M. Eskandari and D. Fathi, *Sci. Rep.*, 2024, **14**, 5500.
15 S. Kar, N. Jamaludin, N. Yantara, S. Mhaisalkar and W. Leong, *Nanophotonics*, 2021, **10**, 2103–2143.
16 H. Wang, A. Treglia, M. Albaqami, F. Gao and A. Petrozza, *ACS Energy Lett.*, 2024, **9**, 2500–2507.
17 M. Zhang, X. Ma, J. Esguerra, H. Yu, O. Hjelm, J. Li and F. Gao, *Nat. Sustainability*, 2025, **8**, 315–324.
18 M. F. Rahman, A. Sur and A. Zubair, *Sol. Energy Mater. Sol. Cells*, 2026, **299**, 114201.
19 X. Shi, Y. Liu, Z. Yuan, X. Liu, Y. Miao, J. Wang, S. Lenk, S. Reineke and F. Gao, *Adv. Opt. Mater.*, 2018, **6**, 1800667.
20 Q. Zhang, D. Zhang, Y. Fu, S. Poddar, L. Shu, X. Mo and Z. Fan, *Adv. Funct. Mater.*, 2020, **30**, 2002570.
21 M. Futscher and B. Ehrler, *ACS Energy Lett.*, 2017, **2**, 2089–2095.
22 C. Chen, Y. Chen, Z. Fang, R. Ge, J. Wu and X. Chen, *APL Photonics*, 2024, **9**, 030903.
23 S. Zainab, M. Azeem, S. Awan, S. Rizwan, N. Iqbal and J. Rashid, *Sci. Rep.*, 2023, **13**, 6954.
24 P. Akhter, M. Huang, W. Spratt, N. Kadakia and F. Amir, *J. Appl. Phys.*, 2015, **117**, 123102.
25 Q.-H. Yang, H.-Q. Wei, G.-H. Li, J.-B. Huang, X. Liu and G.-M. Cai, *Mater. Today Phys.*, 2023, **36**, 101143.
26 J. Li, Y. Ren, Z. Wang and X. Li, *Radiat. Meas.*, 2025, **189**, 107527.
27 L. Lian, M. Zheng, P. Zhang, Z. Zheng, K. Du, W. Lei, J. Gao, G. Niu, D. Zhang, T. Zhai, S. Jin, J. Tang, X. Zhang and J. Zhang, *Chem. Mater.*, 2020, **32**, 3462–3468.
28 Y. Li, P. Vashishtha, Z. Zhou, Z. Li, S. Shivarudraiah, C. Ma, J. Liu, K. Wong, H. Su and J. Halpert, *Chem. Mater.*, 2020, **32**, 5515–5524.
29 S. Yue, S. McGuire, H. Yan, Y. Chu, M. Cotlet, X. Tong and S. Wong, *ACS Omega*, 2019, **4**, 18219–18233.
30 F. Gao and C. Liu, *Opt. Mater.*, 2025, **167**, 117355.
31 Z. Jiang, H. Liu, J. Zou, Y. Huang, Z. Xu, D. Pustovyi and S. Vitusevich, *RSC Adv.*, 2023, **13**, 5993–6001.
32 Y. Wang, X. Wen, P. Ran, C. Peng, F. Yang, Y. Yang and Y. Wu, *Laser Photonics Rev.*, 2025, **19**, 2402302.
33 C. Liu, L. Wang, F. Fang, Z. Zhao, J. Pan, J. Akram, S. B. Shafie, R. Talaighila, Q. Li, Z. Zhao, J. Wu, Z. Zhu, W. Lei, X. Zhang and J. Chen, *Front. Mater.*, 2021, **8**, 682833.
34 X. Wen, Q. Gao, Q. Wang, W. Chewpraditkul, M. Korjik, S. Kurosawa, M. Buryi, V. Babin and Y. Wu, *Opt. Mater.:X*, 2024, **23**, 100335.
35 B. Zhang, X. Wu, S. Zhou, G. Liang and Q. Hu, *Front. Optoelectron.*, 2021, **14**, 459–472.
36 D.-Y. Kim, J.-G. Jung, Y.-J. Lee and M.-H. Park, *Materials*, 2023, **16**, 6317.
37 H. Li, Y. Zhao, J. Lu, J. Feng, J. Zhao, K. Lin, W. Feng, L. Jiang, Z. Wei, Z. Du and Y. Wu, *Small*, 2024, **20**, 2308616.
38 P. Xiong, J. Liao, Z. Wang, Q. Zuo, Y. Dai, J. Wu and C. Tong, *Appl. Phys. Lett.*, 2025, **126**, 023911.
39 C. Ramirez-Gutierrez, H. Martinez-Hernandez, I. Lujan-Cabrera and M. Rodriguez-García, *Sci. Rep.*, 2019, **9**, 14732.
40 N. Tabibifar, M. Eskandari, F. Boroumand, D. Fathi and S. Rahimi, *Sci. Rep.*, 2024, **14**, 29165.
41 X. Ma, N. Youngblood, X. Liu, Y. Cheng, P. Cunha, K. Kudtarkar, X. Wang and S. Lan, *Nanophotonics*, 2021, **10**, 1031–1058.
42 M. Y. Khan, T. Usman, A. Ilyas, A. Hassan, U. Younis, A. Ullah, S. A. Ahmad and A. Al Souwaileh, *Mater. Sci. Semicond. Process.*, 2025, **187**, 109144.
43 M. Y. Khan, M. A. Jehangir, I. E. Lee, Q. Wali, T. Usman, M. Yang and A. Al Souwaileh, *AIP Adv.*, 2025, **15**, 105006.
44 M. A. Jehangir, M. Y. Khan, M. Noman, I. E. Lee, Q. Wali, T. Usman, M. Yang and A. Al Souwaileh, *RSC Adv.*, 2025, **15**, 33708.
45 J. Bueno, A. Jiménez-Solano, M. Anaya and S. Carretero-Palacios, *RSC Adv.*, 2025, **15**, 32497–32508.
46 M. u Ain, N. Asma, R. Ullah, Z. Fatima, A. Illahi and W. Ahmed, *RSC Adv.*, 2024, **14**, 12772–12780.
47 Y. Li, T. Gao, Z. He, C. Shen, S. Zhou, M. Li, D. Zhang, Q. Zhang, Y. Fu, X. Mo, Z. Zhang, W. Bi and Z. Fan, *npj Flex. Electron.*, 2025, **9**, 32.
48 J. Wen, K. Rong, L. Jiang, C. Wen, B. Wu, B. Sa, Y. Qiu and R. Ahuja, *Nano Energy*, 2024, **128**, 109802.
49 J. Googasian and S. Skrabalak, *ACS Phys. Chem. Au*, 2023, **3**, 252–262.
50 A. Taflove, S. Hagness and M. Piket-May, *The Electrical Engineering Handbook*, Elsevier, 2005, pp. 629–670.
51 Z. Zhou, Y. Li, Z. Xing, H. Sung, I. Williams, Z. Li, K. Wong and J. Halpert, *Adv. Mater. Interfaces*, 2021, **8**, 2101471.
52 F. Brivio, K. Butler, A. Walsh and M. van Schilfgaarde, *Phys. Rev. B:Condens. Matter Mater. Phys.*, 2014, **89**, 155204.
53 E. Palik, *Handbook of Optical Constants of Solids*, Academic Press, San Diego, 1985.
54 A. Alnuaimi, I. Almansouri and A. Nayfeh, *J. Comput. Electron.*, 2016, **15**, 1110–1118.
55 E. Purcell, H. Torrey and R. Pound, *Phys. Rev.*, 1946, **69**, 37–38.
56 J.-P. Berenger, *J. Comput. Phys.*, 1994, **114**, 185–200.
57 P. Anger, P. Bharadwaj and L. Novotny, *Phys. Rev. Lett.*, 2006, **96**, 113002.
58 L. Xie, B. Chen, F. Zhang, Z. Zhao, X. Wang, L. Shi, Y. Liu, L. Huang, R. Liu and B. Zou, *et al.*, *Photon. Res.*, 2020, **8**, 768–775.
59 M. L. Ali, M. Khan, M. A. Al Asad and M. Z. Rahaman, *Heliyon*, 2023, **9**, e18816.
60 X. Zheng, J. Huang, Y. Liu, T. Wang, S. Han, Z. Wang, B. Teng and S. Ji, *Adv. Photon. Res.*, 2022, **3**, 2100289.
61 Z. Luo, Q. Li, L. Zhang, X. Wu, L. Tan, C. Zou, Y. Liu and Z. Quan, *Small*, 2020, **16**, 1905226.
62 M. Chen, M. Ju, H. Garces, A. Carl, L. Ono, Z. Hawash, Y. Zhang, T. Shen, Y. Qi, R. Grimm, D. Pacifici, X. Zeng, Y. Zhou and N. Padture, *Nat. Commun.*, 2019, **10**, 16.
63 L. Gu, K. Wen and Q. Peng, *et al.*, *Small*, 2020, **16**, 2001861.

64 E. F. Schubert, *Light-Emitting Diodes*, Cambridge University Press, Cambridge, UK, 2nd edn, 2006.
65 G. Salton, *Automatic Text Processing: The Transformation, Analysis, and Retrieval of Information by Computer*, Addison-Wesley Longman Publishing Co., Inc., Boston, MA, USA, 1989.
66 K. Pearson, *Proc. R. Soc. London*, 1895, **58**, 240–242.
67 P. Mao, C. Liu and X. Li, *et al.*, *Light: Sci. Appl.*, 2021, **10**, 180.
68 J. H. Lee, *et al.*, *Opt. Express*, 2005, **13**, 5864–5870.
69 Z. Y. Ooi, A. Jiménez-Solano and K. Gakowski, *et al.*, *Nat. Commun.*, 2024, **15**, 5802.
70 M. Gajdoš, K. Hummer, G. Kresse, J. Furthmüller and F. Bechstedt, *Phys. Rev. B:Condens. Matter Mater. Phys.*, 2006, **73**, 045112.
71 M. Fox, *Optical Properties of Solids*, Oxford University Press, Oxford, UK, 2nd edn, 2010.
72 S. Saha, A. Sur, L. Saha and M. K. Alam, *Nano Select*, 2025, **6**, e70028.
73 C. Li, Z. Luo, Y. Liu, Y. Wei, X. He, Z. Chen, L. Zhang, Y. Chen, W. Wang, Y. Liu, X. Chang and Z. Quan, *Front. Mater.*, 2021, **8**, 682833.
74 L. Lian, M. Zheng, W. Zhang, L. Yin, X. Du, P. Zhang, X. Zhang, J. Gao, D. Zhang and L. Gao, *Adv. Sci.*, 2020, **7**, 2000195.
75 X. Chen, *et al.*, *Adv. Mater.*, 2025, 2500083.
76 D. Han, H. Shi, W. Ming, C. Zhou, B. Ma, B. Saber, M.-H. Du, X. Chen and Q. Zheng, *Nano Energy*, 2022, **99**, 107391.
77 H. Li, X. Zheng, Y. Liu, Z. Zhang and T. Jiang, *J. Phys. Chem. C*, 2019, **123**, 25359–25365.
78 Q. Li, Z. Xu, J. R. McBride and T. Lian, *Microsyst. Nanoeng.*, 2022, **8**, 5.
79 L. Xu, *et al.*, *Microsyst. Nanoeng.*, 2022, **8**, 5.
80 T. Jun, K. Sim, S. Iimura, M. Sasase, H. Kamioka, J. Kim and H. Hosono, *Adv. Mater.*, 2018, **30**, 1804547.
81 Y. Liu, Y. Jing, J. Zhao, Q. Liu and Z. Xia, *ACS Appl. Mater. Interfaces*, 2020, **12**, 52967–52975.
82 X. Wang, H. Chen, H. Zhang, X. Li, C. Zou, L. Xu and B. Cao, *J. Cent. South Univ.*, 2023, **30**, 2977–2987.
83 Z. He, C. Zhang, R. Meng, X. Luo, M. Chen, H. Lu and Y. Yang, *Nanomaterials*, 2020, **10**, 2364.
84 D. Wang, W. Chan, Z. Zhang, X. Zeng, Z. Hong, Y. Liu, J. Chang, H. Wang, W. Tao and Y. Hao, *Adv. Electron. Mater.*, 2017, **3**, 1700169.